Journal of Geophysical Research: Earth Surface

RESEARCH ARTICLE
10.1029/2018JF004605

The Importance of Combined Tidal and Meteorological Forces for the Flow and Sediment Transport on Intertidal Shoals

P. L. M. de Vet[1,2], B. C. van Prooijen[1], R. A. Schrijvershof[2], J. J. van der Werf[2,3], T. Ysebaert[4,5], M. C. Schrijver[6], and Z. B. Wang[1,2]

[1]Delft University of Technology, Delft, Netherlands, [2]Department of Marine and Coastal Systems, Deltares, Delft, Netherlands, [3]Marine and Fluvial Systems Group, University of Twente, Drienerlolaan, Enschede, Netherlands , [4]NIOZ Royal Institute for Sea Research, Department of Estuarine and Delta Systems, Utrecht University, Yereseke, Netherlands, [5]Wageningen Marine Research, Wageningen University & Research, Wageningen, Netherlands, [6]Rijkswaterstaat, Middelburg, Netherlands

Abstract Estuarine intertidal areas are shaped by combined astronomical and meteorological forces. This paper reveals the relative importance of tide, surge, wind, and waves for the flow and sediment transport on large intertidal shoals. Results of an intensive field campaign have been used to validate a numerical model of the Roggenplaat intertidal shoal in the Eastern Scheldt Estuary, the Netherlands, in order to identify and quantify the importance of each of the processes over time and space. We show that its main tidal creeks are not the cause for the dominant direction of the net flow on the shoal. The tidal flow over the shoal is steered by the water level differences between the surrounding channels. Also during wind events, the tidal flow (enhanced by surge) is dominant in the creeks. In contrast, wind speeds of order 40 times the typical tidal flow velocity are sufficient to completely alter the flow direction and magnitude on an intertidal shoal. This has significant consequences for the sediment transport patterns. Apart from this wind-driven flow dominance during these events, the wind also increases the bed shear stress by waves. For the largest intertidal part of the Roggenplaat, only ~1–10% of the yearly transport results from the 50% least windy tides, even if the shoal is artificially lowered half the tidal range. This dominance of energetic meteorological conditions in the transports matches with field observations, in which the migration of the creeks and high parts of the shoal are in line with the predominant wind direction.

Key Points:
- The geometry of the surrounding channels drive the flow on intertidal shoals; their local morphology only affects the detailed flow patterns
- Wind-driven flow is important on intertidal shoals if the wind speed exceeds about 40 times the tidal flow velocities
- Wind and waves control the sediment transport on these shoals; the water level rising and falling rates control the transport in the creeks

Correspondence to:
P. L. M. de Vet,
p.l.m.devet@tudelft.nl

Citation:
de Vet, P. L. M., van Prooijen, B. C., Schrijvershof, R. A., van der Werf, J. J., Ysebaert, T., Schrijver, M. C., & Wang, Z. B. (2018). The importance of combined tidal and meteorological forces for the flow and sediment transport on intertidal shoals. *Journal of Geophysical Research: Earth Surface*, *123*, 2464–2480. https://doi.org/10.1029/2018JF004605

Received 16 APR 2018
Accepted 15 SEP 2018
Accepted article online 20 SEP 2018
Published online 11 OCT 2018

1. Introduction

Estuarine intertidal shoals are shaped by a combination of different hydrodynamic forces that vary significantly over time and space. Tidal forcing is generally considered as the most important process for intertidal areas, as it imposes variations in water level and velocity (Le Hir et al., 2000). Wind induces a setup or setdown of the water level, a local shear at the surface, and surface waves. All these effects modify the flow and sediment transport rates and are especially effective for (very) shallow water conditions (Green & Coco, 2014; Shi et al., 2017; Talke & Stacey, 2008). Furthermore, bathymetric variations on the intertidal flat and the geometry of the surrounding channels also influence the hydrodynamics. So far, it has been studied insufficiently to what extent each of these mechanisms is dominant for the hydrodynamics and sediment transport of intertidal shoals surrounded by channels.

Intertidal areas can be attached to the shore (fringing flats). For example, the Chongming intertidal flats in the Yangtze Estuary, China (Yang et al., 2001; Zhu et al., 2017), the flats in San Francisco Bay, United States (Talke & Stacey, 2008; Van der Wegen M. et al., 2017), and Baie de Marennes-Oléron, France (Bassoullet et al., 2000; Le Hir et al., 2000). The attachment to the shore has significant consequences for the tidal flow. Especially cross-shore flows are limited by the closed boundary. Those limitations of the flow do not exist for intertidal shoals surrounded by channels, as the water could theoretically flow in any direction. Intertidal shoals are found in estuaries worldwide like the Eastern Scheldt and Western Scheldt, the Netherlands (De Vet, van Prooijen, & Wang, 2017; Van den Berg, 1984; Van den Berg et al., 1996), Yangtze Estuary, China (Gao et al., 2010; Wei et al., 2016), Wadden Sea, the Netherlands (Elias et al., 2012), and Columbia River Estuary, United States (Sherwood et al., 1990). Intertidal shoals surrounded by channels have not been measured as often as fringing flats, possibly because intertidal shoals surrounded by channels are more difficult to access.

There is a growing need for deeper understanding of the hydrodynamics and sediment transport on intertidal shoals, as these areas provide a high ecological value (Smaal & Nienhuis, 1992) and support important ecosystem services (Barbier et al., 2011). To understand the shoals surrounded by channels, complex models, covering the full geometry of the intertidal shoal and its surroundings, need to be applied (Lettmann et al., 2009; Luan et al., 2017). Despite the geometrical differences with fringing flats, the insights on intertidal shoals also benefit the understanding of intertidal areas in general.

However, the processes relevant for intertidal shoals surrounded by channels are not always well resolved. Even in recent modeling studies on the morphodynamics of estuarine shoals, wind, and waves are not always included (e.g., Dam et al., 2016; Van de Lageweg & Feldman, 2018). The inclusion of these processes adds complexity and demands large computational power if the full wind climate and nonidealized geometry are considered (e.g., 118 computational cores in the study of Becherer et al., 2018). Also, (very) high resolution data (in the order of 10 m) are needed to capture the small-scale bathymetry features like local elevation differences and tidal creeks. Such tidal creeks are an essential part of the (de)watering system of intertidal areas and are ecologically valuable (Mallin & Lewitus, 2004). Eisma (1998) provided a classification of tidal creeks. In many cases, tidal creeks are connected to marsh channels, but a presence of a marsh is not a requirement for the existence of a tidal creek. Although tidal creeks are no full cross-connecting channels, they have similarities. Just as cross-connecting channels (Swinkels et al., 2009), tidal creeks can be affected by flows induced by water level gradients between the surrounding channels (Van den Berg, 1986).

This study identifies and assesses the relative importance of the tide, surge, wind, and waves for hydrodynamics and sediment transport on intertidal shoals surrounded by channels. Furthermore, we identify to what extent the flow patterns on such a shoal are driven by its local elevation differences, its tidal creeks, and its surrounding channels. The Roggenplaat, a shoal in the Eastern Scheldt in the Netherlands, is considered as a case. We combine an extensive field campaign, containing 16 Acoustic Doppler Current Profilers (ADCPs), with a numerical model. Instead of modeling the long-term evolution with a prerequisite low resolution, we use a high-resolution (grid size 30 m) model schematization to unravel the hydrodynamic and sediment transport processes from a single tide to a full year. We use elevation data with a high horizontal resolution (< 10 m) such that also the major creeks are well resolved. The different contributions of the processes are unraveled by systematically switching on and off specific processes in the simulations. First, the focus is on the implications on the hydrodynamics. Second, the implications on the sediment transport rates are considered. Finally, the results are extended toward general indicators for intertidal shoals.

2. Methodology

2.1. Description of Roggenplaat Intertidal Shoal

The Roggenplaat, located in the southwest of the Netherlands in the Eastern Scheldt basin (Figure 1a), is an example of a major intertidal shoal surrounded by channels. With an intertidal surface area of 14.6 million m^2, it is the largest intertidal shoal of the Eastern Scheldt. The Roggenplaat is a valuable case to analyze the importance of the different processes, as an extensive data set on morphology and hydrodynamics exists. Two channels surround the shoal; the northern channel is substantially longer and deeper than the southern one (Figure 1f). The Eastern Scheldt is characterized by a typical tidal range of 2.5 m near the mouth, which amplifies up to 3.5 m in the southeast branch of the basin (De Vet, van Prooijen, & Wang, 2017). As the branches of the estuary are closed, there is no river inflow. Around the Roggenplaat, MLW (Mean Low Water) equals MSL-1.2 m (MSL = Mean Sea level) and MHW (Mean High Water) equals MSL+1.3 m. The surge within this area is 50% of the time between −0.11 and +0.14 m but can extend for severe storms to −1 or +1.5 m (2015 data). Typically, the timescale of such an intense surge is 1 day. The shoal is sandy with a median sediment grain size of 210 ± 2.5 μm ($n = 150$), with less than 5% silt (<63 μm) at most locations. Oyster patches (*Crassostrea gigas*) cover 3% (45 ha) of the Roggenplaat. Around these patches more silty sediments are found. After the completion of the storm surge barrier (SSB in Figure 1) and the closure of the branches of the estuary in 1986, the previously accreting Roggenplaat faced severe erosion due to reduced tidal flow within the estuary (De Vet, van Prooijen, & Wang, 2017; Louters et al., 1998). This is a possible threat to the nature value of this Natura 2000 estuary (Ostermann, 1998).

Figure 2 indicates the changes in the geometry of the Roggenplaat complex over past centuries. Around 1827, the complex consisted of various individual intertidal shoals. These smaller intertidal shoals merged into a smaller number of larger intertidal shoals. A similar merging also occurred for the intertidal areas in the Western Scheldt Estuary (Cleveringa & Taal, 2015). With the merging, the complex of flats evolved into two major intertidal areas divided by a major tidal channel: the Roggenplaat and Neeltje Jans. The southern edge of the Roggenplaat faced a 5 to 10 m/year northward retreat, which is still observed in recent years. The two major

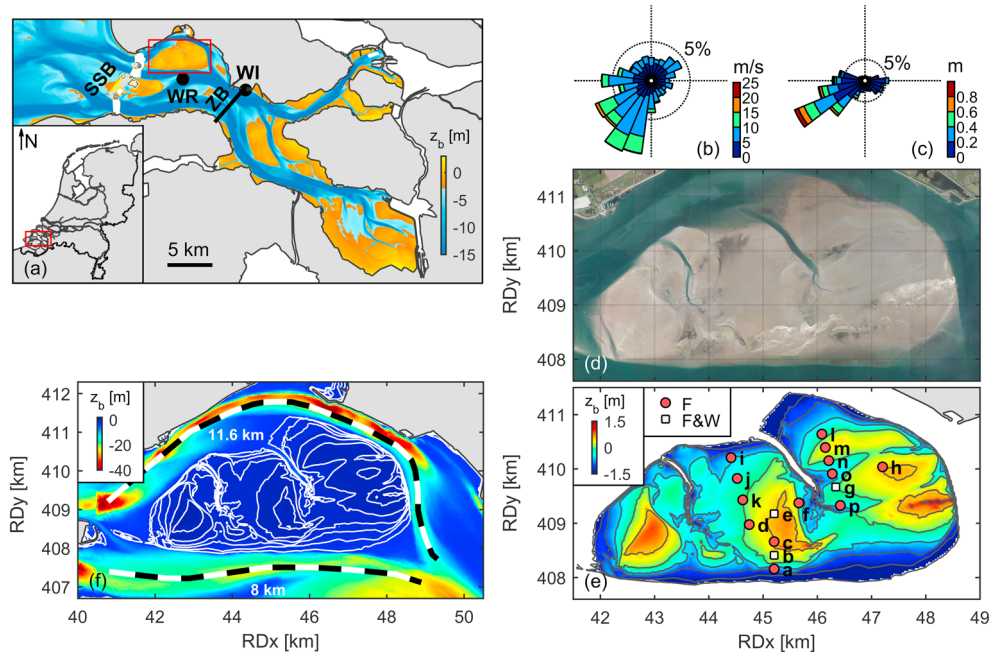

Figure 1. An overview of the Eastern Scheldt is provided in (a) with an indication of the storm surge barrier (SSB), Zeeland Bridge (ZB), wave rider (WR), wind station (WI), and Roggenplaat (red box). The wind rose for 2015 as measured at WI is visualized in (b), and the wave rose for March–December 2015 as measured at WR in (c). An aerial picture of 2014 (courtesy of Cyclomedia) of the Roggenplaat is shown in (d). In (e) the 2013 bathymetric data of the Roggenplaat are visualized with respect to MSL, based on single beam and LiDAR data (source: Rijkswaterstaat). Contour lines are indicated every 0.5 m over the vertical. The locations of the 16 measurement stations (*a*–*p*) are marked of which all stations included an Acoustic Doppler Current Profiler measuring flow (F) and some stations also included a wave logger (F + W). In (f) the bathymetric data are visualized again but now with a color scale focusing on the bathymetry of the surrounding channels. The mentioned distances in (f) indicate the length of the channels along the dashed lines.

tidal creeks of the Roggenplaat, both orientated toward the NW, are former channels which were the division between the different areas of the Roggenplaat complex (Van den Berg, 1984). Figure 2 indicates that the tidal creeks moved in NE direction while decreasing in length. Despite the dynamic historical evolution of the Roggenplaat and the decreased depth and discharge in its creeks (Nio et al., 1980), the creeks still exist and their orientation remained directed toward the NW.

The more recent evolution of the elevation of the Roggenplaat is shown in Figure 3. A clear lowering of the high ridges of the Roggenplaat is visible, in contrast to the accretion before the construction of the barrier (Louters et al., 1998). While lowering, they propagated in N/NE direction, indicated by erosion on the stoss side

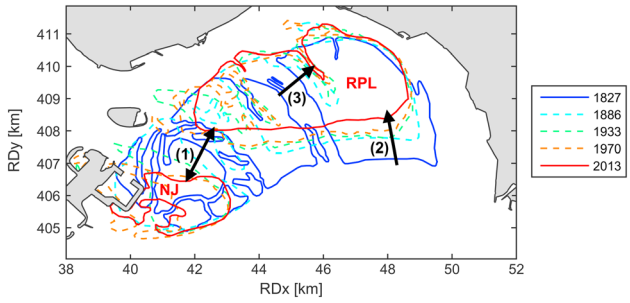

Figure 2. Evolution of the mean low water contour lines of the Roggenplaat complex from 1827 to 2013. Both Roggenplaat (RPL) and Neeltje Jans (NJ) intertidal areas are shown as they were part of the same complex in the past. Contour lines are digitalized based on historical maps (Haring, 1947; Van den Berg, 1986) and for 2013 based on single beam and LiDAR measurements (Marijs & Paree, 2004; Wiegmann et al., 2005). Not all years with data availability are shown to ensure readability. The arrows mark (1) the division between the Roggenplaat and Neeltje Jans, (2) the retreat of the southern edge of the Roggenplaat, and (3) the propagation of the eastern creek.

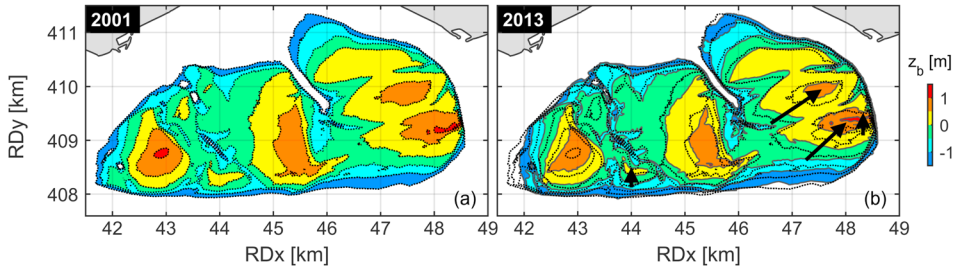

Figure 3. Bathymetry of the Roggenplaat in (a) 2001 and (b) 2013, based on single beam and LiDAR data with respect to mean sea level. The dashed contour lines of the bathymetry of 2001 are also shown in (b) to allow for a comparison between both years. The arrows in (b) indicate the main retreat direction at these locations.

and accretion at the lee side (in addition to a net sand loss). The high ridges in the south are partly covered with dead cockle shells (white patches in the aerial picture of Figure 1d), which faced a similar N/NE propagation pattern over recent years. Currently, the eastern creek is the largest tidal creek of the shoal, with a width exceeding 100 m and an average depth of around 5 m.

2.2. Numerical Model Setup

A numerical model schematization is set up with the package Delft3D (Lesser et al., 2004). The differences in the hydrodynamics between three-dimensional simulations and depth-averaged simulations were small for this case: the different physical processes considered in this study have orders of magnitude larger effects on the residual flow than the errors introduced by the depth-averaged approach. Therefore, the depth-averaged approach is followed in line with prior studies of intertidal areas (e.g., Gong et al., 2012; Le Hir et al., 2000). The model domain extends from the storm surge barrier to the Zeeland Bridge, both indicated in Figure 1a. In Figure 4 the computational grid is shown. Discharges are prescribed on the boundary segments at the storm surge barrier, whereas weakly reflective Riemann invariants (combination of water levels and velocities) are prescribed on the boundary at the Zeeland Bridge. The model is forced on these boundaries with time series of 2015 derived from a nesting procedure in a model covering the full Eastern Scheldt and its outer delta, which is coupled to an even larger model covering a large part of the North Sea (the DCSMv6-ZUNOv4-Kf model schematization; Zijl et al., 2015, 2013). The year 2015 was a representative year for the local wind climate. Some simulations intentionally did not include surge; the surge in those cases was removed from the boundary conditions by considering only astronomical components with harmonic analysis.

The intertidal area of the Roggenplaat is captured with a model grid size of ≈30 m (Figure 4). A simulation with a finer grid size of ≈10 m gave very similar results in hydrodynamics (up to a few centimeter per second differences in the area of interest), which indicates that the ≈30 m resolution is sufficient for this study (and favorable because of approximately 27 times smaller computational times). The bathymetry on the shoal is based on LiDAR (LIght Detection And Ranging) data of 2013, and multibeam data of 2015 were used in the two major tidal creeks. For the rest of the domain, the Vaklodingen data set of 2013 was used, which is a combination of single beam measurements and LiDAR data (Marijs & Paree, 2004; Wiegmann et al., 2005). A uniform Manning roughness of 0.022 s/m$^{1/3}$ was applied over the full domain, which resulted in flow velocities most in line with the observations. For simulations that include sediment transport, the Van Rijn (2007a; 2007b) transport model was used with a median sediment grain size of 210 μm (based on field observations).

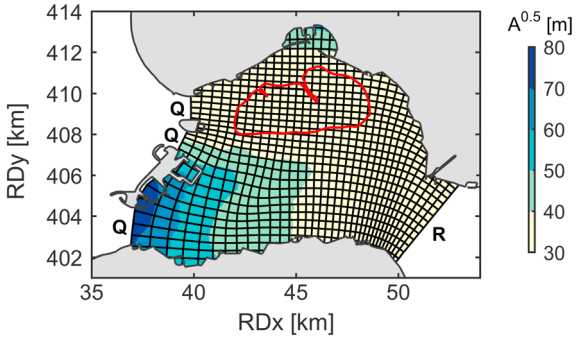

Figure 4. Visualization of the computational grid. One percent of the grid lines are shown to ensure readability. The colors indicate the grid resolution, represented by the square root of the grid cell surface. The boundary containing Riemann segments is marked with R; the boundaries containing discharge segments are marked with Q. The contours of the Roggenplaat are shown as a reference in red.

To assess the importance of waves, a stationary SWAN wave model (2017 version: 41.10; Booij et al., 1999) was coupled to the Delft3D flow model at an interval of 30 min. The wave forces, based on the wave energy dissipation rate, are included in the momentum equations of the flow model. Also, the bed shear stresses in the flow model are enhanced by the waves. Two modifications to the default settings were made to achieve decent results in shallow regions. First, instead of using a constant gamma value (maximum wave height to depth ratio), the β-kd model (Salmon & Holthuijsen, 2015; Salmon et al., 2015) was used, which improved depth-induced wave

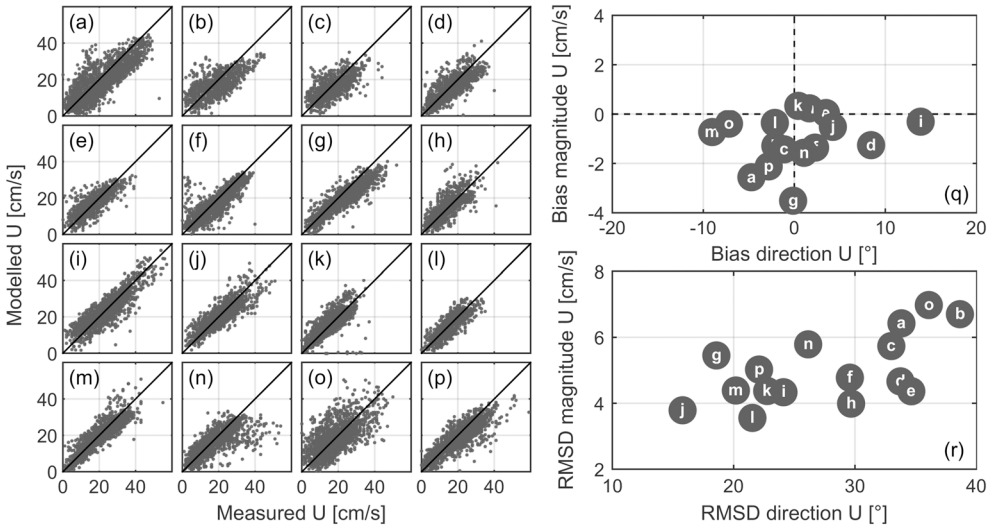

Figure 5. Modeled flow velocity magnitudes compared to measured flow velocity magnitudes for stations *a*–*p* (subfigure letters correspond to station names in Figure 1e). In (*q*) the biases (modeled minus observed) for the magnitude and direction of each station are shown. In (*r*) the root-mean-square deviations (RMSD) between the model results and measurements are presented. All processes (including wind and waves) were enabled in this simulation.

breaking by taking the bottom slope and the normalized wave number into account. This implies a gamma value smaller than 0.73 (minimal 0.54 in this formulation) for mild sloping beds, in line with observations on intertidal areas (e.g., Le Hir et al., 2000). Second, the Madsen roughness model (Madsen et al., 1989) with a 5 cm roughness length scale was applied uniformly over the domain.

2.3. Comparison Between Model Predictions and Field Measurements

Over 1 month (February/March 2015), 16 ADCPs were simultaneously employed in upward looking mode to provide flow velocity measurements on the intertidal shoal. The instruments were placed in four transects as indicated in Figure 1e. Every 10 min, flow velocities were measured and averaged over periods of 400 s with 10 cm bin sizes and blanking. In this study, the ADCP measurements were used to validate the model. No detailed analysis of the time series is provided here.

The model is compared to the flow velocity measurements in Figure 5. The model results are relatively well in line with the measurements; the absolute bias in the magnitude of the velocities is at most 3.5 cm/s, and the absolute bias in direction is less than 14°. The root-mean-squared deviations range between 3.5–7 cm/s and 6–39°. Some local deviations are unavoidable, as real-world spatial irregularities in bed roughness (e.g., due to oyster reef patches that cover part of the shoal) are too complex to take into account and outside the scope of this paper. A variation in various model parameters (e.g., bed roughness and background horizontal eddy viscosity) did not result in better results. Given the relatively small model domain, the quality of the boundary conditions and the high-resolution bathymetric data proved fundamental to describe the flow over the shoal accurately.

Even though extensive field measurements are available for the validation of the model, the validation of individual processes is only possible up to a limited extent. The correlation between the wind and the wind-driven waves (Le Hir et al., 2000) causes the wind-driven flow to occur simultaneously with the

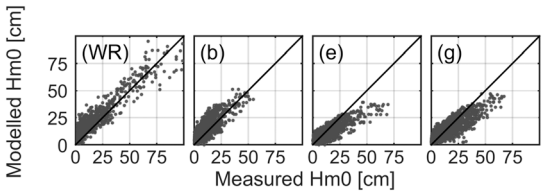

Instrument	WR	b	e	g
Bias	5.1 cm	3.7 cm	-1.5 cm	0.5 cm
RMSD	7.0 cm	5.3 cm	3.8 cm	4.7 cm

Figure 6. Modeled significant wave heights (Hm0) compared to measured significant wave heights for the wave rider (WR) and the available pressure boxes at stations *b*, *e*, and *g* (see Figure 1e for locations) for a 2-month simulation (March and April 2015). The table provides the bias and the root-mean-square deviations (RMSD).

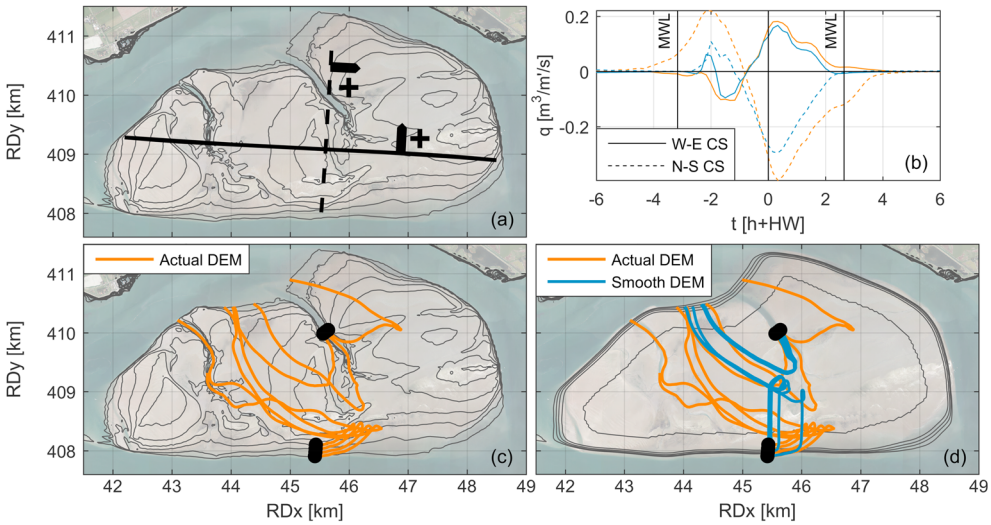

Figure 7. Model results for a typical tidal cycle with mild wind conditions (5 March 2015; wind speeds smaller than 4 m/s). (a) The cross sections considered in this study, with their positive flow directions. The instantaneous discharges per unit width through these cross sections are shown in (b) for both the actual DEM (Digital Elevation Map) as for a smoothed DEM of the shoal (colors match legend of [d]), with the time axis relative to the high water level timing. (c) The tracks of the drogues released at the black dots during rising tide just before MWL for the actual DEM. (d) The same tracks, but additionally, the tracks are shown for the simulation with the smoothed DEM. Black lines indicate elevation contour lines (0.5 m distance). MWL = mean water level.

wave-driven flow. Therefore, only the combined result of the wind- and wave-driven flows is validated with the measurement data.

Since March 2015, a wave rider measured wave characteristics south of the Roggenplaat. Furthermore, for 3 months (February — April 2015) three wave loggers were deployed on the intertidal shoal (5 Hz, OSSI pressure sensors). The locations of the instruments are indicated in Figure 1e. Figure 6 shows a comparison between the modeled and measured wave heights. Especially the higher wave heights are relatively well in line between the model and the measurements. The quality of the model is considered good enough for the desired analyses of this study (bias ranges between −1.5 and 5.1 cm and root-mean-squared deviations between 3.8 and 7.0 cm). Also, the peak periods of the waves are modeled in agreement with the wave logger measurements (bias of −0.2 to −0.5 s and root-mean-squared deviations of 0.2 to 0.4 s). Deviations between the model and measurements are not necessarily the result of model inaccuracies. The translation of pressure fluctuations measured near the bottom to wave heights will also induce inaccuracies (Bishop & Donelan, 1987).

3. Results

We assess the importance of the different processes focusing on the intertidal zone of the shoal and on the major tidal creek. First, we analyze the main driver of the flow on the shoal, for a tide without substantial wind.

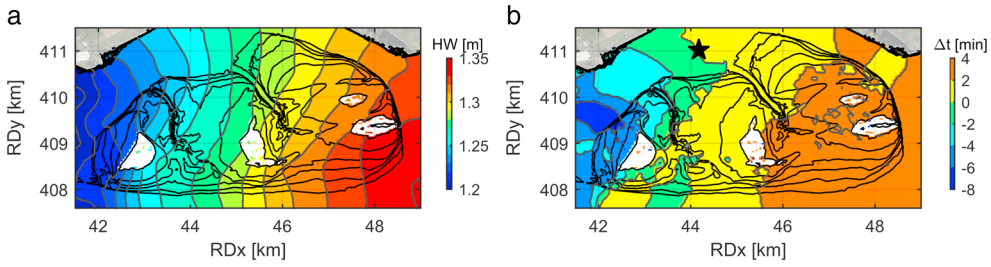

Figure 8. (a) High water level with respect to mean sea level for each computational cell averaged over the high waters of the first half of March 2015. Cells with a bed level higher than the lowest high water level were not considered (white in the figure). (b) The difference in timing of the mean high water level with respect to a reference point (indicated with the star). Black lines indicate elevation contour lines (0.5 m distance).

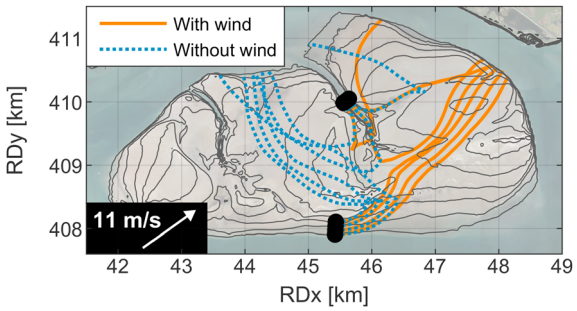

Figure 9. Model results for a tidal cycle with a relatively strong wind (1 March 2015; average wind speed of 11 m/s from SW). Both the drogue tracks for a simulation with and without the wind forcing are shown. Black lines indicate elevation contour lines (0.5 m distance).

Then, the focus is on a tide with strong wind speeds, to assess the consequences of a wind event. To analyze the fluctuations in the importance of the processes over a year, scenarios were set up of full year simulations in which the different processes are included one by one. Finally, sediment transport simulations were run to assess the consequences of the different processes on the transport rates.

3.1. The Driver of the Net Flow on the Shoal Without Wind

To analyze the general pattern of the flow on the shoal, Figure 7b shows the discharges through a W-E and a N-S cross section (indicated in Figure 7a). This is based on a model simulation of a single tide on 5 March 2015, which is a representative tide for calm wind conditions, as the wind did not exceed 4 m/s during the considered tidal cycle. The simulation with the actual bathymetry shows that the flow with rising water levels is mainly directed to the SE, whereas already before HW the flow turns toward the NW. The discharge during the first half of the tidal cycle is substantially smaller compared to the second half, during which high velocities lasted longer. Figure 7c shows that this net NW discharge of water over the shoal is well visualized by a simulation of drogues, released during rising water levels just before MWL (mean water level). The drogues released in the tidal creek are initially steered in SE direction onto the shoal but then driven to the NW where they leave the shoal toward the northern channel. The drogues released at the southern edge of the intertidal shoal are driven onto the intertidal area during the inundation phase and then also face a net NW movement with the strong flow speeds occurring after HW.

The bathymetry of the intertidal shoal is characterized by two NW orientated tidal creeks which are surrounded by relatively low regions compared to the rest of the intertidal area; see Figure 1e. To test whether the net NW flow is a consequence of these NW orientated lower regions on the intertidal shoal, the simulation is repeated for a fully flattened and smoothed bathymetry of the intertidal area; the rest of the system is left unchanged. Figure 7d shows the tracks of the drogues for both the actual bathymetry, and the flattened and smoothed one (height of MSL+0.0 m, equal to the average height of the actual bathymetry). Differences in the pathways of the drogues between both simulations are visible (with the smoothed bathymetry the drogues are less dispersive), but the net NW movement of all drogues is still clearly there. This is also expressed well by the discharges through the cross sections for the smoothed bathymetry in Figure 7b. Also, differences are visible here, mainly around or below MWL where the smoothed bathymetry fully submerges and especially in the N-S transect where the tidal creek is part of. But also, the net NW movement is still strongly visible in this flattened and smoothed bathymetry. Therefore, the local bathymetry definitely affects the detailed flow patterns, but it is certainly not the main cause for the net NW flow on the intertidal shoal. Contrariwise, the tidal creeks may result from the main flow.

Without substantial meteorological influences, the flow on the shoal is driven by water level gradients and bed friction. A regular tidal analysis (e.g., Pawlowicz et al., 2002) is not possible for intertidal areas because of discontinuous time series every tide. Instead, Figure 8a shows the spatial distribution of the average high water levels over the model domain. Apart from providing insights in the gradients on the shoal, such an analysis is suitable for this study as the timing of the NW flow coincides with HW (see Figure 7). Although water level gradients can also follow by spatial differences in the timing of the tides, Figure 8b indicates that these differences in timing are limited (order of minutes) compared to the tidal period. Hence, the spatial distribution of the high water levels is a good indicator for the water level gradients around high water. Although not everywhere with exactly the same direction, Figure 8a shows that the water level gradients on the shoal are directed to the NW/NWW on the largest part of the area (mainly in the center and east part of the shoal). This is in line with the net flow direction over the shoal (e.g., Figure 7). The isolines of the high water levels indicate that the northwestern gradient is caused by differences in high water levels along the surrounding channels. The differences in water level gradients in both surrounding channels originate from differences in the geometry of both channels. The northern curved channel is substantially longer (11.5 km) and deeper compared to the shorter (8 km) and almost straight southern channel (Figure 1f). Differences in tidal propagation are hence a necessary consequence, also because both channels are connected to each other and, therefor, have a similar water level east and west of the shoal.

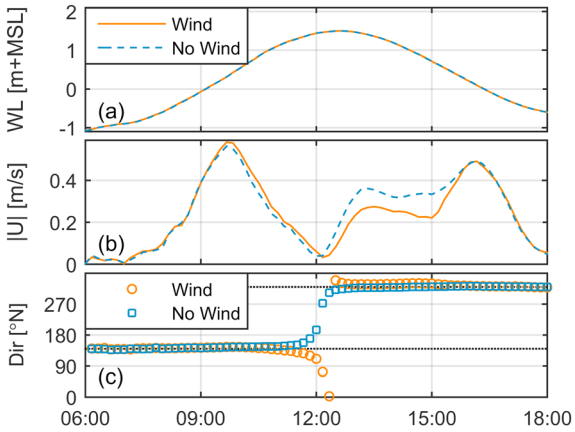

Figure 10. Time series of water level elevation (a), depth-averaged flow velocity magnitude (b), and direction (c), modeled in the center of the eastern tidal creek (same location as the released drifters in Figure 9). Similar as in Figure 9, the tide of 1 March is considered in a simulation with wind (average wind speed of 11 m/s from SW) and without wind. In (c) the orientation of the channel axis is marked with the black dashed lines.

3.2. The Impact of a Single Wind Event on the Flow

To analyze whether the previous observations are also representative for days with more severe wind speeds, a tide that coincided with a strong wind is considered (1 March, wind speeds on average 11 m/s from SW). Figure 9 shows the tracks of the drogues modeled both for a simulation with the actual wind climate and for a simulation without any wind forcing. Although the tidal range of this specific tide is different compared to the previously considered tide, the tracks for the case without wind forcing are very similar to the results of 5 March which was characterized by limited wind speeds (compare Figure 9 to Figure 7c). However, when the simulation with the actual wind climate of 1 March is considered, the drogue tracks are substantially different. With the inclusion of such a wind event, the main flow on the shoal is well in line with the governing wind direction (NE directed) and hence not in the NW direction as observed in cases without wind.

Figure 10 shows the flow velocity through the eastern tidal creek for this tide of 1 March. Similar to Figure 9, both a simulation with and without the presence of the wind is considered, to assess the effect of such a wind event on the depth-averaged flow in a tidal creek. Apart from a very short period around high water slack, the flow in the creek is less affected by the wind compared to the flow on the shoal (Figure 9). Still, the wind causes deviations in flow velocities up to 10 cm/s during the considered tide. However, the peak velocities in the creek are almost unaffected by the presence of the wind (<3 cm/s and <2° deviation), as these peaks occur around MWL. Around MWL, the intertidal area is not fully inundated, hindering a full flow over the shoal (see Figure 1e). Also, the direction of the flow in the creek, aligned with the channel axis during substantial flow velocities, is only slightly affected by the wind.

3.3. Fluctuations Over a Year

Previous sections have shown that the tides result in a net flow in NW direction, but that wind can change this pattern. To determine whether this modification is a result of the surge, wind-induced shear stress, or wave-induced flow a set of simulations is carried out to unravel these contributions. A full year (2015) is simulated, with each simulation different processes enabled: (T) tide only; (T + S) tide and surge; (T + S + Wi) tide, surge, and wind-induced shear stress; and (T + S + Wi +Wa) tide, surge, wind-induced shear stress, and wave forces. Comparing the different simulations, the added contribution of each process can be assessed. To visualize the result, the net discharge through the cross-sections W-E and N-S (see Figure 7a) was determined per tidal cycle and plotted as a function of the high water level of that tide in Figure 11.

First, only astronomical tidal signals were imposed on the boundaries of the model domain. In this case, a possible surge was filtered out by means of a tidal analysis (Pawlowicz et al., 2002) and wind and waves were not imposed. Figure 11 shows always a positive flux for the W-E cross section and a negative flux for the N-S cross section. This indicates a net discharge always directed to the northwest if the model is only enforced by tides. Furthermore, an almost linear relationship is found between the high water level of each tide and the net discharge over the shoal during that tide ($R2 = 0.73$ for the W-E cross section and 0.95 for the N-S cross section). The results are very similar if the actual surge is imposed: a larger range of high water levels coincides

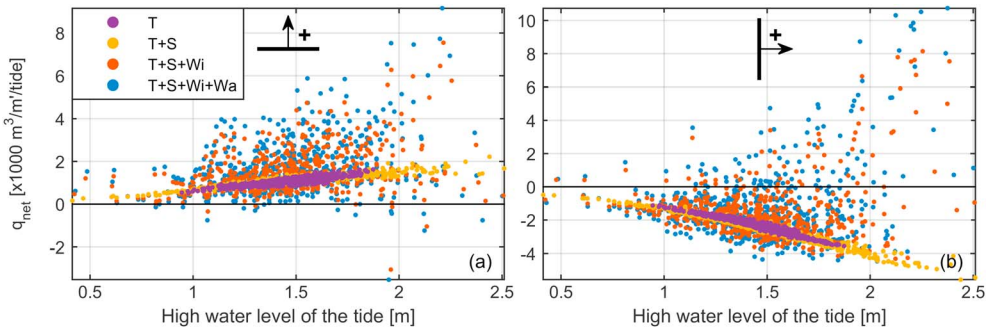

Figure 11. Net flow discharges per tide through the (a) W-E and (b) N-S cross sections as defined in Figure 7a. Every dot represents the net discharge through the cross section versus the high water level (with respect to mean sea level) for each single tide. Four different simulations are considered with different processes enabled: (T) tide only; (T + S) tide and surge; (T + S + Wi) tide, surge, and wind; and (T + S + Wi + Wa) tide, surge, wind, and waves. Results are based on simulations of the full year 2015.

with a larger range of net discharges. Still, the almost linear relationship holds ($R2 = 0.87$ for the W-E cross section and 0.97 for the N-S cross section) and all considered tides have a net discharge toward the NW.

The results are substantially more scattered with the inclusion of the wind forcing (waves still omitted). For the simulation with tides and surge, the standard deviation of the net discharge was 264 m^3/m'/tide for the W-E cross section and 800 m^3/m'/tide for the N-S cross section. With wind forcing, these increase to 936 and 1,596 m^3/m'/tide, respectively. The wind is capable of fully altering the direction of the main flow, as also concluded from Figure 9. The almost linear relationship no longer holds. The deviation from the simulation with only tides and surge increases substantially for higher high water levels, and for the highest high water levels there are even more tides with a net discharge to the east than to the west. This is due to the correlation between wind speeds and water levels (through the wind-induced surge). Finally, the scatter increases slightly more if also waves are included in the model simulation due to wave-induced flow. The standard deviation of the net discharge equals now to 1,216 m^3/m'/tide for the W-E cross section and to 2,051 m^3/m'/tide for the N-S cross section. Such a net wave-induced flow is similarly observed for shallow reefs (Symonds et al., 1995). Because waves are mainly locally generated in this area, the direction of the wave-induced flow is generally in line with the direction of the wind-induced flow.

The discharges of each individual tide are now related to the average wind speed of each tide for the simulation including all processes in Figure 12, to better understand the scatter found in Figure 11. The scatter does increase not only with higher high water levels (as observed in Figure 11) but also strongly with increasing wind speeds. Together with the magnitude of the wind speed, the wind direction is another strong indicative parameter for the discharge over the area (Figure 12).

Especially for large wind speeds, the flow over the shoal is driven by the wind. The net discharge is directed to the NW for all considered tides with a wind speed smaller than 7 m/s, whereas the net discharge is directed to the NE for all considered tides with a wind speed larger than 13 m/s. The limited variation in net flow direction during high wind speeds (e.g., no net western flow for high wind speeds) is a consequence of the local wind climate. SW is namely the only direction where these strong winds originated from in 2015 (see Figure 1b). Still, there were some tides with moderate winds from the NW for which the net northward flow was substantially reduced or even a net SE directed flow was the result.

In conclusion, the wind results in surge, wind-induced flow, and wave-induced flow. Although there is a relation between the high water level and the discharge over the shoal, it is especially the wind-driven flow that is responsible for the fluctuations in the net flow over the considered year.

3.4. Implications of the Different Processes on the Sediment Transport Rates

So far, we focused on the importance of local bathymetry and the different forcing mechanisms on the residual flow over the shoal. Now, the focus is on the impact of each of these processes on the sediment transport rates. We consider an individual tide, to rule out the complexity induced by wind speeds and directions changing all year long. Again, the tide of 1 March is considered which was characterized by relatively strong wind speeds (on average 11 m/s from the southwest; see Figure 9).

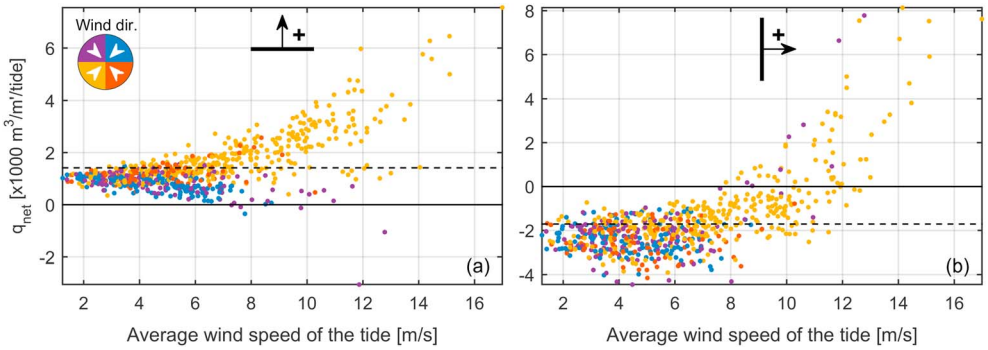

Figure 12. Net flow discharges per tide through the (a) W-E and (b) N-S cross sections as defined in Figure 7a. Every dot represents the net discharge through the cross section versus the average wind speed for each single tide. The colors indicate the direction of the wind for each tide. Results are based on a simulation of full 2015 including all processes (tide, surge, wind, and waves). The dashed line represents the yearly averaged tidal discharge.

In Figure 13, the net sediment transport rates on the shoal are shown (with the Van Rijn, 2007a, 2007b, transport model), for simulations with the inclusion of all processes and also with the exclusion of waves, wind, or surge. The main transport is in NE direction for the simulation with all processes (Figure 13a). This is in line with the prevailing wind direction. For the higher regions of the shoal, a consequential NE propagation of the bed profile can be deduced by the increasing transport rates at the stoss side and decreasing transport rates on the lee side of those high elevated regions (especially visible around $RDx = 47$ km and $RDy = 410.5$ km). The bed level changes are, namely, the direct result of the divergence in the sediment transport fluxes. There is a substantial spatial variability in hydrodynamic forcing and hence in sediment transport present over the intertidal shoal. At the edges of the shoal, the largest transport rates are observed as a consequence of the relatively high flow velocities and the substantial wave breaking processes. In the creek, the net transport rates are substantially smaller during this wind event.

If waves are disabled (Figure 13b), the net transport rates on the intertidal shoal are several orders of magnitude smaller (also orders of magnitude smaller compared to the rates in the creek). This implies that waves are crucial for the sediment transport on this intertidal area. In contrast to the wind, apart from a flow, waves also induce (as visualized in Figure 11) additional stirring of the sediment by velocity fluctuations near the bed. However, this does not imply that the other processes are irrelevant. In fact, the sediment transport rates on the shoal are highly reduced if the wind is disabled while waves are still imposed (Figure 13c). The wind itself is

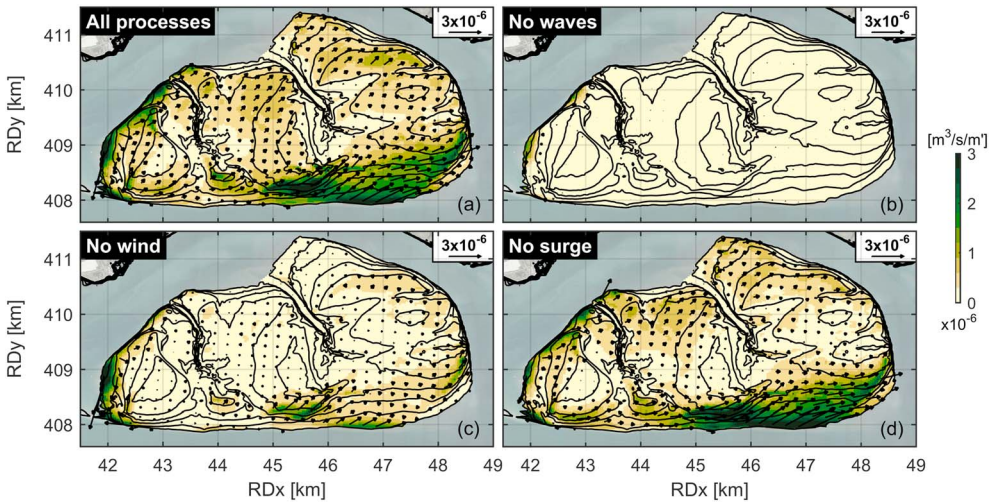

Figure 13. Mean total transport rates (bed load + suspended load) in the intertidal zone of the shoal for (a) including all processes, (b) excluding only waves, (c) excluding only wind, and (d) excluding only the surge for a tidal cycle with a relatively strong wind (1 March 2015; average wind speed of 11 m/s from SW). Only the transport rates on the shoal (for bed elevations higher than 2 m below mean water level, i.e., slightly below mean low water) and within the tidal creeks (all depths) are visualized to improve clarity. For the same reason, only 1/36th of the modeled arrows are shown.

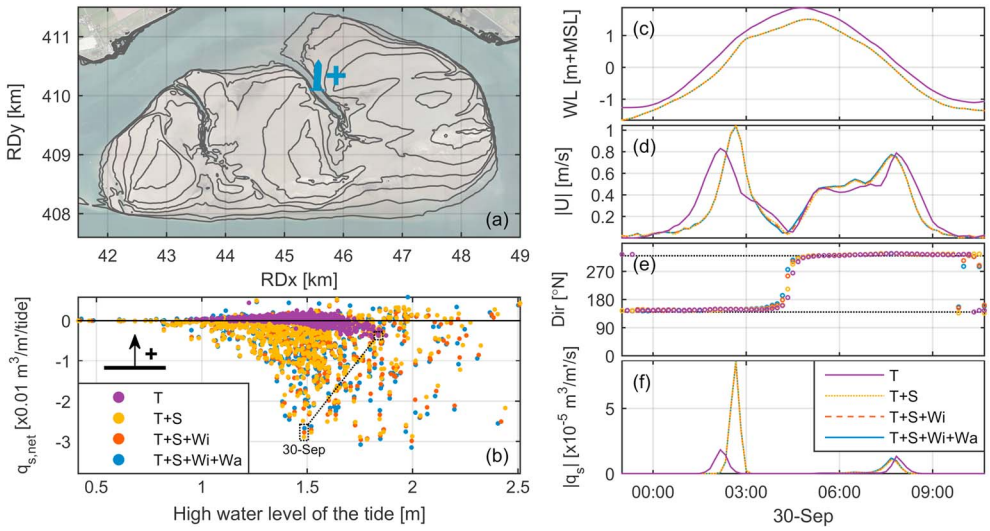

Figure 14. The net total (bed load + suspended load) sediment discharge for each tide as a single dot versus the high water level for each single tide in (b), for a W-E cross section in the eastern tidal creek as indicated in (a). Similar to Figure 11, four different simulations of the full year 2015 are considered with different processes enabled: (T) tide only; (T + S) tide and surge; (T + S + Wi) tide, surge, and wind; and (T + S + Wi + Wa) tide, surge, wind, and waves. For each simulation, the water level (c), depth-averaged flow velocity magnitude (d), velocity direction (e), and total sediment transport magnitudes (f) are visualized for the deepest point of the cross section for the tide of 30 September as marked also in (b). In (e) the orientation of the channel axis is indicated with the black dashed lines.

hence an important amplifier of the sediment transport rates by affecting the flow on the shoal. When similarly only the surge is not considered (Figure 13d), the transport rates are also slightly reduced but substantially less compared to the case without wind.

The major tidal creeks on the intertidal area are characterized by lower bed levels (around MWL-5 m) and consequently larger depths than on top of the shoal. Therefore, the relative importance of the tide, wind, and wave processes for the sediment transport rates is not necessarily the same for these creeks as for the shoal. Figure 10 already showed that flow velocities in the eastern creek are hardly affected by wind events. To test the importance of the different processes for the sediment transport rates in the eastern tidal creek, the sediment transport rates through a cross section are analyzed in Figure 14.

If only the tidal forcing is imposed (Figure 14b), the net sediment transport direction in the creek is mainly directed to the north for relatively small high water levels and mainly directed to the south for relatively large high water levels. More importantly, the net transport rates are highly different if the surge is also included now. For similar high water levels, the net transport rates can be an order of magnitude larger. Although higher high water levels result in a larger variation in the net transports, the high water level does not provide a direct relation with the magnitude of the net sediment transport rates itself. The spread changes slightly when also the wind or both the wind and the waves are included. But this is of minor importance compared to the impact of the surge on the sediment transport rates.

The hydrodynamics and sediment transport in the center of the cross section are analyzed in more detail for a single tide in Figures 14c–14f. The focus is now on the tide of 30 September, as it is a good example of a tide with much higher net sediment transport rates if all processes are considered compared to the tide-only simulation, more than a factor of 7 difference (see Figure 14b). This tidal cycle is characterized by a wind speed of 6 m/s from ENE direction. First, Figure 14c indicates a setdown in the estuary of 0.35 m for this specific tidal cycle. Nevertheless, the peak flood velocity is larger with the inclusion of the surge/setdown (Figure 14d) which imposed significantly larger magnitudes of flood sediment transport rates (Figure 14f). These larger peak velocities are the direct consequence of the faster rising rate of the water level around MWL when the surge is included (Figure 14c), the surge affects hence the asymmetry of the tidal wave. Because the surge imposes a setdown, the timing of the flow velocity and sediment transport peaks is altered, but Figure 14e indicates that the direction of the flow is still in line with the channel axis. Only around slack water, some

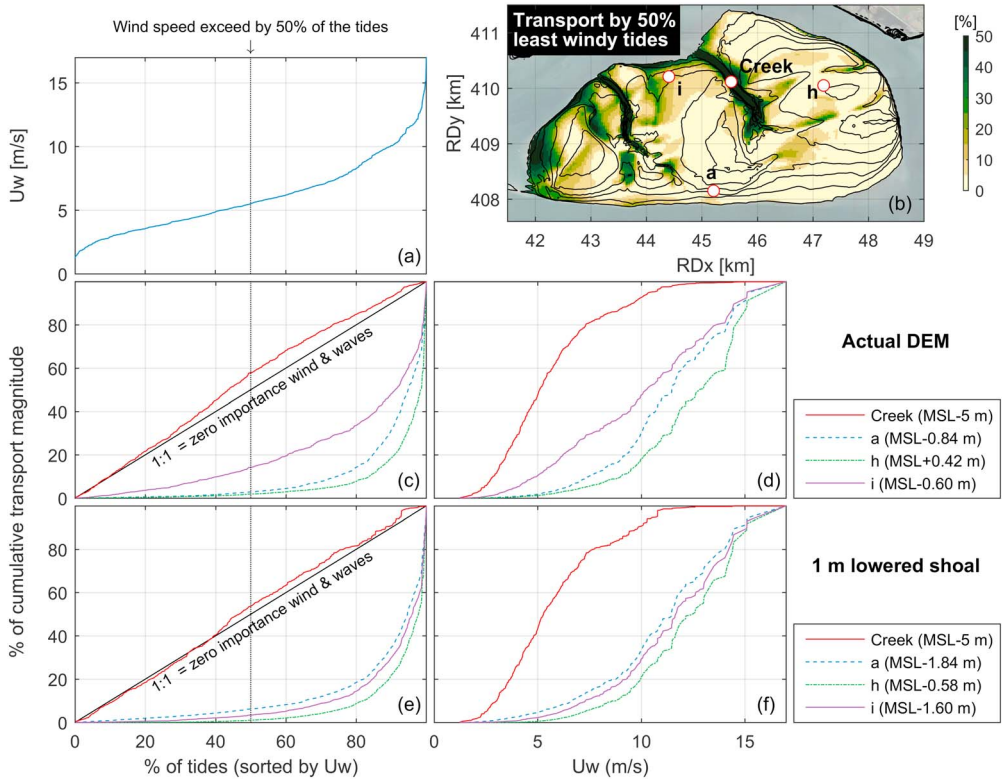

Figure 15. Quantification of the role of meteorological processes on the sediment transport rates on the shoal, based on a full year simulation including all processes. (a) The distribution of wind speed. The percentage of the cumulative sediment transport magnitude, in which the tides are sorted by the wind speed, is presented for the actual bathymetry in (c) as a function of the percentage of the tides and in (d) as a function of the wind speed. The same is presented in (e) and (f) after lowering the shoal with 1 m (only original cells above MWL-2 m). Panel (b) visualizes for the actual bathymetry the percentage of the cumulative transport magnitude that is generated by the 50% least windy tides, matching the vertical dotted line in (c) and (e). Furthermore, (b) also visualizes the location of the observation points of the other graphs, in line with Figure 1e.

deviations in direction are visible, but these are with the low velocities irrelevant for the sediment transport. The inclusion of wind, even together with the waves, does not imply any consequences for the sediment transport rates in these deep parts of the creek, in line with the already minor impact of a stronger wind event in Figure 10 on the hydrodynamics in the creek.

Figures 15c and 15d quantify the relative importance of the wind and waves on the cumulative transport magnitude at various locations for a simulation of a full year. In line with Figure 14, the wind and waves hardly affect the transport in the creek. Contrarily, the transport rates on the largest part of the intertidal shoal are strongly dominated by the wind and waves as the tides with the 50% lowest wind speeds (<5.5 m/s) only explain ~1–10% of the yearly transport (see also Figure 15b). These tides determine only 3% of the transport at point *a* (exposed edge of the shoal). At point *i* (sheltered edge of the shoal) wind and waves are slightly less important as these tides determine still 14% of the transport. Further away from the channel and for higher elevations, the relative importance of the wind and waves increases (points *j* and *k*). The largest relative dominance by the wind and waves is found for the highest elevations at the center of the shoal, for example, at point *h* less than 2% of the sediment is transported by the tides with the 50% lowest wind speeds.

To test how sensitive the dominance of the meteorological processes is to the height of the shoal, we lowered the shoal 1 m. This is roughly half the tidal amplitude (i.e., cells around MWL became roughly MLW), and only cells that were above MWL-2 m are lowered. Figures 15e and 15f show the cumulative sediment transport for this lowered shoal. After the lowering, the meteorological forcing is still essential for the shoal. The creek is still tide dominated. The transport processes at point *a*, which is highly exposed to wave attack, are slightly less dependent on the extreme meteorological conditions. The water depth is larger, and waves are therefore less effective. Point *i* is more influenced by extreme wind conditions. The shoal is longer

submerged, and wind can therefore play a role over a longer period. The simulations with the real bathymetry and the lowered shoal show that the exact bed level is not essential for the dominance of the wind. Wind dominance on tidal shoals can therefore be expected for a variety of shoals and is not only important on the Roggenplaat.

In conclusion, the combination of waves and wind determines the sediment transport rates in the intertidal zone of the shoal. Contrarily, the rising and falling rate of the water level determines the transport rates in the deep creek. There is hence a major spatial variability in the importance of the different processes.

4. Discussion

Hydrodynamic processes on an intertidal shoal appeared to be a complex outcome of tidal and meteorological (i.e., surge, wind, and waves) forcing mechanisms that strongly vary over time and space. Therefore, to understand sediment transport on such an intertidal shoal, the importance of each of these processes has to be considered both in space and time.

4.1. Temporal Variations

The relative importance of the different hydrodynamic forcing mechanisms varies on different timescales. First, the flow on an intertidal shoal is diverse in magnitude and direction over an individual tidal cycle, still with a clear dominant net direction (e.g., Figure 7). Second, spring-neap variations cause variations in the magnitude of the flow over the shoal while leaving the orientation of the net flow unchanged (Figure 11). Other time fluctuations are related to meteorology. Meteorological events have a direct impact on the water level setup within the estuary, the wind-driven flow, and the wave-driven flow. A water level setup has a similar consequence as a higher astronomical high water level (Figure 11): an amplification of the magnitude of the flow without a substantial change in directions. In contrast, the locally generated wind- and wave-driven flows can alter both the magnitude and the direction of the flow on the shoal.

These, partly independent, temporal fluctuations shall have consequences for the long-term evolution of intertidal shoals. As sediment transport on the relatively sandy Roggenplaat takes place especially during energetic meteorological events (Figure 15), as also observed on other intertidal areas (e.g., Green et al., 1997; Van der Werf et al., 2015), those events are likely fundamental for the morphological evolution of such a shoal. In strong contrast to astronomical fluctuations, these meteorological events are not deterministic. Still, the wind climate (Figure 1b) provides important insights in the long-term fate of an intertidal shoal. Meteorological events capable of altering the flow (Figure 9) are not rare for the Roggenplaat area: 12.5% of the time wind speeds exceeded 10 m/s in 2015. Furthermore, these events have a clear dominant direction, well in line with the historical net propagation of the creeks and the bed features on the shoal. Still, the impact of individual meteorological events depends on the timing of these with respect to other time fluctuations (e.g., timing within an individual tidal cycle and within the spring-neap cycle). The existence of those different time fluctuations provides direct challenges for long-term modeling studies, in which simplification of the forcing mechanisms (e.g., meteorological climate) is required to save computational times.

4.2. Spatial Variations

The relevance of the different processes varies strongly on the shoal. It is shown that especially the tide and the surge dominate the flow velocities and sediment transport in the tidal creeks. The orientation of the tidal creeks is well aligned with the net flow over the shoal imposed by the tide and the surge. Similar to cross-connecting channels (Swinkels et al., 2009), differences in the tidal wave propagation, dependent of the geometry of the surrounding channels (e.g., Figure 1f), are found to drive the flow direction. The shape of the tidal wave is crucial for the velocity in the creeks, specifically the fastest rising and falling rates. Wind and waves are only of minor importance in the creeks because of the relatively large water depths (to exclude depth-induced breaking of waves, i.e., ~2 times the maximum significant wave height in the creeks) and large flow velocities (characteristic peak flow in the considered creeks is ~1 m/s which dominates over the wind-driven flow), in contrast to what was found on the shoal. Still, storms might affect the creeks when sediments transported on the shoal get trapped in the creeks. In this case the creeks will migrate in line with the main sediment transport direction on the shoal, as a consequence of gradients in sediment transport. On the shoal, the tide and surge are also relevant for the hydrodynamics during calm weather conditions. However, the wind and waves during energetic meteorological events are clearly the dominant processes for the sediment transport in the intertidal zone of the shoal. Under calm weather conditions, the flow velocities on the shoal are too small to induce substantial sediment transport rates, as waves are crucial for stirring the sediment.

Apart from a distinction between the creeks and the intertidal zone of the shoal, also, over the shoal itself differences in the importance of the processes are present. As the net flow is a consequence of the geometry of the surrounding channels, it depends on the location on the shoal on how strong this gradient is and in which direction this is precisely pointed. Specifically for the Roggenplaat, Figure 8a indicates that this gradient is especially predominantly NW orientated on the center and east side of the shoal. On the west part, the gradients are more orientated to the west, as the water levels in the surrounding channels are more aligned around there. Also, the contribution of waves is not homogeneous over space for intertidal areas (also stressed by Green & Coco, 2014). A large fraction of the wave dissipation occurs at the edges of the intertidal area, imposing relatively large transport rates locally there, which coincides for the Roggenplaat with the region which faced the main erosion over the past (Figures 2 and 13d). The high-resolution output of the model allows for a spatial decomposition of the shoal in various zones. Figure 15b visualizes the percentage of the cumulative transport magnitude that is generated by the 50% least windy tides for each cell. In combination with Figure 13, and in line with the analyses of the points in section 3.4, various zones are identified: (1) tidal creeks, which are strongly tide dominated; (2) high ridges on the shoal with transport mainly during meteorological events; (3) exposed side (southern edge), which is wave dominated; (4) sheltered tide-dominated side (W/NW of the shoal), which is sheltered and only tide dominated; and (5) sheltered wind-dominated side (E/NE of the shoal), which is not exposed to waves and mainly influenced by wind-driven flow.

4.3. General Indicators

This study unraveled the relative importance of the processes for the Roggenplaat in detail. The insights are applicable beyond this specific case. For example, this holds for the crucial combined role of wind and waves on intertidal shoals. Morphodynamic studies, which do not consider these processes at all (e.g., Dam et al., 2016; Van de Lageweg & Feldman, 2018), hence have a limited predictive capacity on the intertidal shoals. This especially holds for the higher parts of the shoals. Furthermore, the insights on the driving mechanisms for the flow and sediment transport result in general indicators for other shoals. These are especially valuable if data are limited.

We suggest that by considering several basic indicators, the large-scale hydrodynamics and sediment transport on an intertidal shoal can be understood qualitatively without the need of thorough model simulations. First, geometrical features visible on satellite imagery indicate the orientation of the main flow on a shoal during mild wind conditions. The orientation of major tidal creeks is a good indicator for the main flow direction as meteorological events are of less importance for the orientation of these creeks. Also, the difference in length between the surrounding channels and their shape is, through the resulting water level gradients, indicators of the main flow. Second, a local wind rose can indicate a dominant transport direction for the high elevations of a shoal, as the transport rates on these high areas are highly affected by wind events and the related waves. Strong indications follow especially if a clear dominant wind direction is present.

To determine whether wind is important on tidal shoals, we make a first-order estimate. We consider the one-dimensional depth-averaged momentum equation and start for a wind-only situation (no tides). For shallow water, weak flow gradients, and limited temporal gradients, we can neglect the time variation of the velocity and the advective part of the momentum equations and reach a balance between three terms:

$$\rho_w g d \frac{\partial h}{\partial x} - \tau_{\text{wind}} + \rho_w c_f u |u| = 0 \tag{1}$$

where ρ_w is the density of water, g the gravitational acceleration, d the water depth, $\frac{\partial h}{\partial x}$ the water level gradient, τ_{wind} the wind shear stress, c_f the dimensionless friction coefficient, and u the flow velocity. If we simplify this equation further by neglecting the pressure gradient term, we get a balance between the wind shear stress and the bed shear stress. Such a simplification is possible if the wind cannot result in an extra buildup of a pressure gradient. This is approximately the case for a shoal surrounded by channels, in which the return flow in its surrounding channels does not accommodate the pressure gradient buildup. Similarly, such pressure gradient cannot build up along an alongshore uniform fringing flat. Approximating the simplified balance between the wind shear stress and the resisting friction force with typical values (wind drag coefficient C_D ranges between 0.001 and 0.002 for wind speeds 10 m from the surface U_{10} of 5–20 m/s, an air density ρ_a of 1.23 kg/m^3, and c_f of 0.003) leads to the following:

$$0 = \tau_{\text{wind}} - \rho_w c_f u|u| = \rho_a c_D U_{10}|U_{10}| - \rho_w c_f u|u| \tag{2}$$

$$U_{10} = \sqrt{\frac{\rho_w c_f}{\rho_a c_D}} u \tag{3}$$

$$U_{10} \approx \sqrt{\frac{1000 \cdot 0.003}{1.23 \cdot 0.0015}} u \approx 40\, u \tag{4}$$

This factor of 40 is a first-order estimate of the wind-only velocity and should be considered with care. It is not intended as a predictor of the precise wind-driven flow velocity, as the resulting velocity is not simply the sum of the tide-only velocity and the wind-only velocity (see equation (1)). However, if the wind-only velocity is in the same order as (or especially if even larger than) the tide-only velocity, then the wind-only velocity definitely makes a significant contribution to the resulting velocity. Therefore, it is a simple indicator to determine for a shoal (or fringing flat in alongshore direction), based on the wind speed and the governing tidal velocity, whether wind is an important process to be considered. The results of the Roggenplaat showed that the factor of 40 is in the right order of magnitude. For this shoal with typical tidal velocities of 0.25 m/s (e.g., Figure 5), wind speeds in the order of 10 m/s and higher were sufficient to modify the net flow patterns substantially; see Figures 9 and 12.

Every intertidal area is unique; still its uniqueness is the result of the same processes. The relative importance of the wind and waves on the sediment transport rates for other shoals depends on local characteristics (also sediment grain size), just as it also varies spatially over a single tidal shoal (e.g., Figure 15). In general, the larger the impact of wind and waves on the sediment transport rates, the further the curve in Figure 15c will be positioned to the bottom right corner, while tide-dominated areas will result in straighter lines in this graph. The latter holds for tidal creeks or edges of the shoal which are sheltered from waves but subject to a strong forcing from the channel. Shoals that inundate every tide allow the wind to alter the direction of the flow in any direction. In case a land boundary is present (i.e., for fringing flats), the degrees of freedom for the net flow direction are reduced. For such fringing flats, an alongshore pressure gradient in the channel or an alongshore directed wind stress will still affect the flow, similarly as shown in this study for an intertidal shoal. On intertidal shoals surrounded by channels with limited tidal flow velocities, smaller than several decimeters per second as on the Roggenplaat, only minor winds are required to affect the flows (e.g., Christiansen et al., 2006). But even for intertidal areas with large tidal flow velocities, there are phases in each tidal cycle during which strong winds will control the flow, for example, during slack water. Therefore, we emphasize that the wind should generally be included in (modeling) studies on intertidal areas.

5. Conclusions

In the absence of wind, the net flow on an intertidal shoal surrounded by channels is primarily driven by water level gradients between its surrounding channels. These water level gradients depend on the geometry of these channels. The local bathymetry of the shoal and its tidal creeks influences the local details of the flow patterns. The tidal creeks are mainly important for the inundation and dewatering of the shoal when the water level is rapidly changing and the water depth on the shoal is limited. Higher high water levels, for example, due to spring-neap variations and storm surges, amplify the discharge over a shoal. Nevertheless, the rising and falling rates of the water level dominate the variability of the flow and transport in the creeks, not the height of the high water level. Wind and waves do not substantially affect the flow and transport in such creeks.

Wind is a crucial driver for the hydrodynamics and sediment transport on the intertidal shoals surrounded by channels. First, the wind-generated waves are key for the sediment transport in such environments. Second, strong wind and waves impose a net flow well in line with the governing wind direction. This is especially the case if the wind speed exceeds about 40 times the typical tidal velocity (based on a momentum balance), which occurs at least frequently around slack water. These two aspects indicating the crucial role of the wind explain that the bed profile on the shoal propagated in the main wind direction in the observations. There are regions slightly less affected by wind and waves, for example, the relatively sheltered edge of the shoal with relatively high tidal flow velocities and especially the deep tidal creeks. But the sediment transport on the intertidal shoal is clearly dominated by wind and waves, even in the less exposed areas of the shoal. In the investigated case, only ~1–10% of the transport was induced by the 50% least windy tides on the largest part of the shoal. Even an artificial 1 m lowering of the shoal (roughly half the mean tidal range) did not weaken the dominance of the meteorological processes on the shoal, highlighting the generic importance of the results. This emphasizes that the combination of waves and wind should always be considered in analyses and simulations of intertidal shoals.

Acknowledgments
This work was supported by the Netherlands Organisation for Scientific Research (NWO) via the project *EMERGO - Eco-morphological functioning and management of tidal flats* (850.13.021). The data presented in this paper are surveyed by Rijkswaterstaat, apart from the three wave loggers which were deployed by NIOZ. We thank Cyclomedia for providing the aerial pictures. The Delft3D model schematization applied in this paper was developed in close collaboration with Deltares, within the Roggenplaat Nourishment Project (project number 1220324, part of Center of Expertise Delta Technology) commissioned by Rijkswaterstaat. The model data for this paper are made available on the online 4TU data repository as De Vet, van Prooijen, Schrijvershof, et al. (2017). We gratefully acknowledge the Editor (Giovanni Coco), the Associate Editor (Ton Hoitink) and the three anonymous reviewers for their constructive comments.

References

Barbier, E. B., Hacker, S. D., Kennedy, C., Koch, E. W., Stier, A. C., & Silliman, B. R. (2011). The value of estuarine and coastal ecosystem services. *Ecological Monographs*, *81*(2), 169–193. https://doi.org/10.1890/10-1510.1

Bassoullet, P., Le Hir, P., Gouleau, D., & Robert, S. (2000). Sediment transport over an intertidal mudflat: Field investigations and estimation of fluxes within the "Baie de Marenngres-Oleron" France). *Continental Shelf Research*, *20*(12-13), 1635–1653. https://doi.org/10.1016/S0278-4343(00)00041-8

Becherer, J., Hofstede, J., Gräwe, U., Purkiani, K., Schulz, E., & Burchard, H. (2018). The Wadden Sea in transition—Consequences of sea level rise. *Ocean Dynamics*, *68*(1), 131–151. https://doi.org/10.1007/s10236-017-1117-5

Bishop, C. T., & Donelan, M. A. (1987). Measuring waves with pressure transducers. *Coastal Engineering*, *11*(4), 309–328. https://doi.org/10.1016/0378-3839(87)90031-7

Booij, N., Ris, R. C., & Holthuijsen, L. H. (1999). A third-generation wave model for coastal regions: 1. Model description and validation. *Journal of Geophysical Research*, *104*(C4), 7649–7666. https://doi.org/10.1029/98JC02622

Christiansen, C., Vølund, G., Lund-Hansen, L. C., & Bartholdy, J. (2006). Wind influence on tidal flat sediment dynamics: Field investigations in the Ho Bugt, Danish Wadden Sea. *Marine Geology*, *235*(1-4), 75–86. https://doi.org/10.1016/j.margeo.2006.10.006

Cleveringa, J., & Taal, M. (2015). A smooth Scheldt, *E-proceedings of the 36th IAHR World Congress* (pp. 22–25). The Hague: IAHR.

Dam, G., van der Wegen, M., Labeur, R. J., & Roelvink, D. (2016). Modeling centuries of estuarine morphodynamics in the Western Scheldt estuary. *Geophysical Research Letters*, *43*, 3839–3847. https://doi.org/10.1002/2015GL066725

De Vet, P. L. M., van Prooijen, B. C., Schrijvershof, R. A., van der Werf, J. J., Ysebaert, T., Schrijver, M. C., & Wang, Z. B. (2017). Data files for Numerical Delft3D model of the Roggenplaat. https://doi.org/10.4121/uuid:6223ad1b-6162-445e-ba61-23fb7fca2d92

De Vet, P. L. M., van Prooijen, B. C., & Wang, Z. B. (2017). The differences in morphological development between the intertidal flats of the Eastern and Western Scheldt. *Geomorphology*, *281*, 31–42. https://doi.org/10.1016/j.geomorph.2016.12.031

Eisma, D. (1998). *Intertidal deposits: River mouths, tidal flats, and coastal lagoons*, pp. 544. Boca Raton: CRC Press.

Elias, E. P. L., van der Spek, A. J. F., Wang, Z. B., & de Ronde, J. (2012). Morphodynamic development and sediment budget of the Dutch Wadden Sea over the last century. *Netherlands Journal of Geosciences*, *91*(03), 293–310. https://doi.org/10.1017/S0016774600000457

Gao, A., Yang, S. L., Li, G., Li, P., & Chen, S. L. (2010). Long-term morphological evolution of a tidal island as affected by natural factors and human activities, the Yangtze estuary. *Journal of Coastal Research*, *261*, 123–131. https://doi.org/10.2112/08-1052.1

Gong, Z., Wang, Z. B., Stive, M. J. F., Zhang, C., & Chu, A. (2012). Process-based morphodynamic modeling of a schematized mudflat dominated by a long-shore tidal current at the Central Jiangsu Coast, China. *Journal of Coastal Research*, *285*, 1381–1392. https://doi.org/10.2112/JCOASTRES-D-12-00001.1

Green, M. O., Black, K. P., & Amos, C. L. (1997). Control of estuarine sediment dynamics by interactions between currents and waves at several scales. *Marine Geology*, *144*(1-3), 97–116. https://doi.org/10.1016/S0025-3227(97)00065-0

Green, M. O., & Coco, G. (2014). Review of wave-driven sediment resuspension and transport in estuaries. *Reviews of Geophysics*, *52*, 77–117. https://doi.org/10.1002/2013RG000437

Haring, J. (1947). Diepteveranderingen in de ooster-schelde over de periode 1827-1933-1947 (Tech. Rep.) Den Haag: Ministerie Van Verkeer En Waterstaat Rijkswaterstaat, Directie Benedenrivieren.

Le Hir, P., Roberts, W., Cazaillet, O., Christie, M., Bassoullet, P., & Bacher, C. (2000). Characterization of intertidal flat hydrodynamics. *Continental Shelf Research*, *20*(12-13), 1433–1459. https://doi.org/10.1016/S0278-4343(00)00031-5

Lesser, G. R., Roelvink, J. A., van Kester, J. A. T. M., & Stelling, G. S. (2004). Development and validation of a three-dimensional morphological model. *Coastal Engineering*, *51*(8-9), 883–915. https://doi.org/10.1016/j.coastaleng.2004.07.014

Lettmann, K. A., Wolff, J.-O., & Badewien, T. H. (2009). Modeling the impact of wind and waves on suspended particulate matter fluxes in the East Frisian Wadden Sea (Southern North Sea). *Ocean Dynamics*, *59*(2), 239–262. https://doi.org/10.1007/s10236-009-0194-5

Louters, T., van den Berg, J. H., & Mulder, J. P. M. (1998). Geomorphological changes of the Oosterschelde tidal system during and after the implementation of the delta project. *Journal of Coastal Research*, *14*(3), 1134–1151.

Luan, H. L., Ding, P. X., Wang, Z. B., & Ge, J. Z. (2017). Process-based morphodynamic modeling of the Yangtze Estuary at a decadal timescale: Controls on estuarine evolution and future trends. *Geomorphology*, *290*, 347–364. https://doi.org/10.1016/j.geomorph.2017.04.016

Madsen, O. S., Poon, Y.-K., & Graber, H. C. (1989). Spectral wave attenuation by bottom friction: Theory, *Coastal engineering 1988*. New York, NY: American Society of Civil Engineers, pp. 492–504. https://doi.org/10.1061/9780872626874.035

Mallin, M. A., & Lewitus, A. J. (2004). The importance of tidal creek ecosystems. *Journal of Experimental Marine Biology and Ecology*, *298*(2), 145–149. https://doi.org/10.1016/S0022-0981(03)00356-3

Marijs, K., & Paree, E. (2004). Nauwkeurigheid vaklodingen westerschelde en -monding "de praktijk" (*Tech Rep*). Vlissingen. (in Dutch).

Nio, S.-D., van den Berg, J. H., Goesten, M., & Smulders, F. (1980). Dynamics and sequential analysis of a mesotidal shoal and intershoal channel complex in the Eastern Scheldt (southwestern Netherlands). *Sedimentary Geology*, *26*(1-3), 263–279. https://doi.org/10.1016/0037-0738(80)90014-7

Ostermann, O. P. (1998). The need for management of nature conservation sites designated under Natura 2000. *Journal of Applied Ecology*, *35*(6), 968–973. https://doi.org/10.1111/j.1365-2664.1998.tb00016.x

Pawlowicz, R., Beardsley, B., & Lentz, S. (2002). Classical tidal harmonic analysis including error estimates in MATLAB using T TIDE. *Computers &, Geosciences*, *28*(8), 929–937. https://doi.org/10.1016/S0098-3004(02)00013-4

Salmon, J. E., & Holthuijsen, L. H. (2015). Modeling depth-induced wave breaking over complex coastal bathymetries. *Coastal Engineering*, *105*, 21–35. https://doi.org/10.1016/j.coastaleng.2015.08.002

Salmon, J. E., Holthuijsen, L. H., Zijlema, M., van Vledder, G. P., & Pietrzak, J. D. (2015). Scaling depth-induced wave-breaking in two-dimensional spectral wave models. *Ocean Modelling*, *87*, 30–47. https://doi.org/10.1016/j.ocemod.2014.12.011

Sherwood, C. R., Jay, D. A., Bradford Harvey, R., Hamilton, P., & Simenstad, C. A. (1990). Simenstad historical changes in the Columbia River estuary. *Progress in Oceanography*, *25*(1-4), 299–352. https://doi.org/10.1016/0079-6611(90)90011-P

Shi, B., Cooper, J. R., Pratolongo, P. D., Gao, S., Bouma, T. J., Li, G., et al. (2017). Erosion and accretion on a mudflat: The importance of very shallow-water effects. *Journal of Geophysical Research: Oceans*, *122*, 9476–9499. https://doi.org/10.1002/2016JC012316

Smaal, A. C., & Nienhuis, P. H. (1992). The eastern Scheldt (the Netherlands), from an estuary to a tidal bay: A review of responses at the ecosystem level. *Netherlands Journal of Sea Research*, *30*, 161–173. https://doi.org/10.1016/0077-7579(92)90055-J

Swinkels, C. M., Jeuken, C. J. L., Wang, Z. B., & Nicholls, R. J. (2009). Presence of connecting channels in the Western Scheldt estuary. *Journal of Coastal Research*, *253*, 627–640. https://doi.org/10.2112/06-0719.1

Symonds, G., Black, K. P., & Young, I. R. (1995). Wave-driven flow over shallow reefs. *Journal of Geophysical Research*, *100*(C2), 2639. https://doi.org/10.1029/94JC02736

Talke, S. A., & Stacey, M. T. (2008). Suspended sediment fluxes at an intertidal flat: The shifting influence of wave, wind, tidal, and freshwater forcing. *Continental Shelf Research*, *28*(6), 710–725. https://doi.org/10.1016/j.csr.2007.12.003

Van Rijn, L. C. (2007a). Unified view of sediment transport by currents and waves. I: Initiation of motion, bed roughness, and bed-load transport. *Journal of Hydraulic Engineering*, *133*(6), 649–667. https://doi.org/10.1061/(ASCE)0733-9429(2007)133:6(649)

Van Rijn, L. C. (2007b). Unified view of sediment transport by currents and waves. II: Suspended transport. *Journal of Hydraulic Engineering*, *133*(6), 668–689. https://doi.org/10.1061/(ASCE)0733-9429(2007)133:6(668)

Van de Lageweg, W., & Feldman, H. (2018). Process-based modelling of morphodynamics and bar architecture in confined basins with fluvial and tidal currents. *Marine Geology*, *398*, 35–47. https://doi.org/10.1016/J.MARGEO.2018.01.002

Van den Berg, J. H. (1984). Morphological changes of the ebb-tidal delta of the Eastern Scheldt during recent decades. *Geologie en Mijnbouw*, *63*(4), 363–375.

Van den Berg, J. (1986). Aspects of sediment- and morphodynamics of subtidal deposits of the Oosterschelde (Netherlands) (Phd thesis), Utrecht University.

Van den Berg, J. H., Jeuken, C. J. L., & Van der Spek, A. J. F. (1996). Hydraulic processes affecting the morphology and evolution of the Westerschelde estuary. In K. F. Nordstrom & C. T. Roman (Eds.), *Estuarine shores: Evolution, environment and human alterations* (Vol. 7, pp. 157–184). Chichester, UK: John Wiley.

Van der Wegen M., Jaffe, B., Foxgrover, A., & Roelvink, D. (2017). Mudflat morphodynamics and the impact of sea level rise in South San Francisco Bay. *Estuaries and Coasts*, *40*(1), 37–49. https://doi.org/10.1007/s12237-016-0129-6

Van der Werf, J., Reinders, J., van Rooijen, A., Holzhauer, H., & Ysebaert, T. (2015). Evaluation of a tidal flat sediment nourishment as estuarine management measure. *Ocean & Coastal Management*, *114*, 77–87. https://doi.org/10.1016/j.ocecoaman.2015.06.006

Wei, W., Mei, X., Dai, Z., & Tang, Z. (2016). Recent morphodynamic evolution of the largest uninhibited island in the Yangtze (Changjiang) estuary during 1998–2014: Influence of the anthropogenic interference. *Continental Shelf Research*, *124*, 83–94. https://doi.org/10.1016/j.csr.2016.05.011

Wiegmann, N., Perluka, R., Oude Elberink, S., & Vogelzang, J. (2005). Vaklodingen: De inwintechnieken en hun combinaties: Vergelijking tussen verschillende inwintechnieken en de combinaties ervan (Tech. Rep.). Delft: Adviesdienst Geo-Informatica En ICT (AGI). (in Dutch).

Yang, S.-L., Ding, P.-X., & Chen, S.-L. (2001). Changes in progradation rate of the tidal flats at the mouth of the Changjiang (Yangtze) river, China. *Geomorphology*, *38*(1-2), 167–180. https://doi.org/10.1016/S0169-555X(00)00079-9

Zhu, Q., van Prooijen, B. C., Wang, Z. B., & Yang, S. L. (2017). Bed-level changes on intertidal wetland in response to waves and tides: A case study from the Yangtze River Delta. *Marine Geology*, *385*, 160–172. https://doi.org/10.1016/j.margeo.2017.01.003

Zijl, F., Sumihar, J., & Verlaan, M. (2015). Application of data assimilation for improved operational water level forecasting on the northwest European shelf and North Sea. *Ocean Dynamics*, *65*(12), 1699–1716. https://doi.org/10.1007/s10236-015-0898-7

Zijl, F., Verlaan, M., & Gerritsen, H. (2013). Improved water-level forecasting for the Northwest European Shelf and North Sea through direct modelling of tide, surge and non-linear interaction. *Ocean Dynamics*, *63*(7), 823–847. https://doi.org/10.1007/s10236-013-0624-2